

TRANSLIENT: DETECTING TRANSIENTS RESULTING FROM POINT SOURCE MOTION OR ASTROMETRIC ERRORS

OFER SPRINGER^{1,2}, ERAN O. OFEK^{1,*}, BARAK ZACKAY¹, RUSLAN KONNO¹, AMIR SHARON¹, GUY NIR³, ADAM RUBIN⁴, ASAF HADDAD¹, JONATHAN FRIEDMAN¹, LEORA SCHEIN LUBOMIRSKY⁶, IAKOV AIZENBERG⁵, ALEXANDER KRASSILCHTCHIKOV¹, AVISHAY GAL-YAM¹,

Submitted to AJ

ABSTRACT

Detection of moving sources over complicated background is important for several reasons. First is measuring the astrophysical motion of the source. Second is that such motion resulting from atmospheric scintillation, color refraction, or astrophysical reasons is a major source of false alarms for image subtraction methods. We extend the Zackay, Ofek, & Gal-Yam image subtraction formalism to deal with moving sources. The new method, named TRANSLIENT (translational transient) detector, applies hypothesis testing between the hypothesis that the source is stationary and that the source is moving. It can be used to detect source motion or to distinguish between stellar variability and motion. For moving source detection, we show the superiority of TRANSLIENT over the proper image subtraction, using the improvement in the receiver-operating characteristic curve. We show that in the small translation limit, TRANSLIENT is an optimal detector of point source motion in any direction. Furthermore, it is numerically stable, fast to calculate, and presented in a closed form. Efficient transient detection requires both the proper image subtraction statistics and the TRANSLIENT statistics: when the transient statistic is higher, then the subtraction artifact is likely due to motion. We test our algorithm both on simulated data and on real images obtained by the Large Array Survey Telescope (LAST). We demonstrate the ability of TRANSLIENT to distinguish between motion and variability, which has the potential to reduce the number of false alarms in transients detection. We provide the TRANSLIENT implementation in Python and MATLAB.

Subject headings: methods: analytical — methods: data analysis — methods: statistical — techniques: image processing — surveys

1. INTRODUCTION

Detection and measurement of sub-pixel motions of sources in astronomical images is required for two major science cases: (i) Detecting motion due to any kind of astrometric noise, or astrophysical motion, that leads to subtraction artifacts seen in image differencing methods, and in turn, leads to false alarms in transient detection; (ii) Measuring astrophysical motion, including proper motion and parallax measurement, detecting astrometric binaries (e.g., Malkov et al. 2012), astrometric microlensing (e.g., Paczyński 1998; Gould 2000; Lu et al. 2016; Sahu et al. 2017; Ofek 2018), lensed quasars (Springer and Ofek 2021a, Springer and Ofek 2021b), binary quasars (e.g., Liu 2015, Shen et al. 2019), and studying the black hole in the center of our Galaxy

(e.g., Ghez et al. 2005; Gillessen et al. 2009).

Although point-spread function (PSF) fitting (e.g., Stetson 1987; Schechter et al. 1993) is an excellent approach for measuring point source positions, and hence, their motion, it is biased in the presence of a complicated background (e.g., in galaxies). Due to their ability to work in complicated background regions, image subtraction algorithms are the method of choice for transient detection (e.g., Phillips and Davis 1995; Alard and Lupton 1998; Bramich 2008; Zackay et al. 2016). Historically, image differencing resulted in subtraction artifacts, non-Gaussian noise, and excess noise compared to the expectation. Some of these problems were solved by the Zackay et al. (2016) (ZOGY) algorithm, which provides an optimal, anti-symmetric, fast, with correct noise propagation, and numerically stable solution to the transient detection problem. Indeed, the application of ZOGY results in a reduced amount of false alarms, sometimes by two orders of magnitude, compared to older methods.

However, some of the assumptions in the derivation of all the existing methods are still not accurate (see discussions in Zackay et al. 2016). One such assumption, which is the subject of this paper, is that the reference image and the new image are perfectly registered. The breakdown of this assumption is yet another leading reason for the presence of false alarms in transient detec-

¹ Department of particle physics and astrophysics, Weizmann Institute of Science, 76100 Rehovot, Israel.

² Benin School of Computer Science and Engineering, The Hebrew University of Jerusalem, 9190416 Jerusalem, Israel.

³ Lawrence Berkeley National Laboratory, 1 Cyclotron Road, MS 50B-4206, Berkeley, CA 94720, USA

⁴ European Southern Observatory, 85748 Garching bei München, Germany.

⁵ QST Financial Group, 4130 Limassol, Cyprus.

⁶ Department of chemical and biological physics, Weizmann Institute of Science, 76100 Rehovot, Israel.

* Corresponding Author: eran.ofek@weizmann.ac.il

tion. In practice, the breakdown of this assumption is unavoidable for several reasons: (i) For ground-based observations atmospheric scintillation shifts the position of stars by an amount typically larger than the measurement error due to the Poisson noise. Furthermore, these shifts are correlated within the < 1 arcmin-size isoplanatic patch, meaning that in practice the stars' positions are shifted, (almost) randomly, with respect to their mean position. (e.g., Lindegren 1980; Shao and Colavita 1992; Ofek 2019). (ii) Color refraction in the atmosphere or in a telescope, along with the variance of stars' colors, introduces variations in the relative positions of stars, as a function of the airmass or the focal plane position, respectively (see e.g., Zackay et al. 2016). (iii) Poisson errors are limiting the accuracy of image registration; and (iv) Proper motion of astrophysical objects.

Zackay et al. (2016) suggested two methods to deal with these astrometric errors. The first method is to propagate the measured (global or regional) astrometric noise of the image into the image subtraction formula. This approach does not attempt to measure motion, but only to ignore flux residuals which may be due to shifts in source positions between the new and the reference images. Zackay et al. (2016) demonstrated the ability of this approach to deal with astrometric errors. A disadvantage of this method is that it is sub-optimal, and requires knowledge about the local astrometric errors⁸. If for example, the displacement of a source between the new and reference images is larger than the assumed astrometric noise, the displaced source will likely generate a detection in the subtraction image. The second suggestion made in Zackay et al. (2016), was to model the flux residual due to a specific astrometric shift in the position of a source by modifying the PSF of one of the images to account for the astrometric misalignment. This suggestion has not been derived and implemented as of yet and is the subject of this paper.

In the current work, we derive a formalism for the detection and measurement of a moving point source on a general static background. Additionally, we prove that in the small translation limit, our detector is an optimal detector of point source motion in any (non-specific) direction. This property is what essentially enables the employment of the discussed method as a blind detection scheme and not as a post-fitting scheme. We also discuss the extent to which small translations can be distinguished from local flux changes and find a set of non-degenerate observational parameters for this task. We refer to the translational transient detection method presented below by the name TRANSLIENT and to transient events arising from point source motion as *translients* (translational transients). This paper deals with deriving the formalism and testing the new method on simulated and real data.

The structure of the paper is as follows: In §2 we develop a statistical image formation model, derive an optimal statistic to perform hypothesis testing in the motion-only scenario, and derive the likelihood of observing a particular difference image when both motion

and a change of flux are taking place. The statistical sufficiency of this difference image is discussed in Appendix A. In §3 we use simulated images to measure the performance of a *translient* detector as compared to the *proper subtraction* detector at various levels of background noise and translation size. We additionally use these simulations to assess the ability to differentiate between motion and flux variation when translations are smaller than the PSF size. In §4 we present some tests of *translient* on real astronomical images, in §5 we describe our software implementations, and we conclude in §6.

2. METHODS DERIVATION

Extending Zackay et al. (2016), we derive the formalism needed to detect and measure point sources moving on a general static background. In §2.1 we outline the employed statistical model of formation of astronomical images. We start by discussing the case of a particular motion in §2.2, and continue with the case of a general motion (direction and amplitude) in §2.3. Next, in §2.4 we discuss how one can distinguish between flux variation and motion, and in §2.5 we present a method to fit the motion and flux variation simultaneously.

2.1. Image formation model

Our model for the reference image (R) and the new image (N) is given by:

$$R = (T + \alpha_r \delta_{\vec{q}}) \otimes P_r + \epsilon_r, \quad (1)$$

$$N = (T + \alpha_n \delta_{\vec{p}}) \otimes P_n + \epsilon_n. \quad (2)$$

Here \otimes denotes convolution, T is a general unknown true background image, r and n subscripts indicate the reference image and the new image, respectively, α_r and α_n are the observed point source fluxes, P_r and P_n are the point-spread-functions (PSF), and $\delta_{\vec{q}}$ and $\delta_{\vec{p}}$ denote Dirac delta functions centered at image positions \vec{q} and \vec{p} , in the reference and new image, respectively. The additive background noise of the images are ϵ_r and ϵ_n and these are assumed to contain independent and identically distributed (i.i.d.) per-pixel Gaussian noise having zero mean and known variances, σ_r^2 and σ_n^2 , respectively. This assumption is typically valid since in most cases astronomical images are in the background-noise-dominated regime, therefore, σ_r and σ_n can be approximated as scalars. Furthermore, the background is high enough such that the Gaussian noise approximation holds (see Ofek and Zackay 2018 for matched filtering in the Poisson noise case). We further assume that the images are Nyquist sampled⁹, and are flux matched¹⁰.

2.2. Detecting pure motion for particular translation

We now specialize our model to the case where we assume that the point source has a constant flux ($\alpha_r = \alpha_n \equiv \alpha$). At each reference image position \vec{q} we would

⁸ Typically, the astrometric errors obtained from the astrometric solutions are based on the global rms. However, because the isoplanatic scale may be smaller than the typical angular distance between stars, the astrometric noise is mostly uncorrelated and may change as a function of spatial position.

⁹ A PSF that has a two-dimensional Gaussian shape, is not band limited. However, in practice, the information content in the edges of the Fourier Transform of the Gaussian is small, and for practical reasons, it is enough to assume that the PSF full-width at half-maximum (FWHM) is about $\gtrsim 2.3$ pixels (see e.g., the effect on astrometry in Ofek (2019)).

¹⁰ In the notation of the Zackay et al. (2016) algorithm this means that $F_r = F_n = 1$.

like our detector to test between the following two hypotheses:

$$\mathcal{H}_0 : \vec{q} = \vec{p}, \quad (3)$$

$$\mathcal{H}_1 : \vec{q} \neq \vec{p}, \quad (4)$$

where the null hypothesis means that the point source is static in both images R and N . Note that a static point source can equivalently be absorbed into the background image T . The alternative hypothesis \mathcal{H}_1 states that a point source, existing in image R at position \vec{q} , has translated to position \vec{p} in the image N .

Motivated by the Neyman-Pearson lemma¹¹ (Neyman and Pearson 1933), and following ZOGY, we express the likelihood-ratio of the alternative and the null hypotheses¹²

$$\begin{aligned} LR(q; p, \alpha) &= \frac{P(N, R | \mathcal{H}_1)}{P(N, R | \mathcal{H}_0)} \\ &= \frac{P(N | R, \mathcal{H}_1) P(R | \mathcal{H}_1)}{P(N | R, \mathcal{H}_0) P(R | \mathcal{H}_0)} \\ &= \frac{P(N | R, \mathcal{H}_1)}{P(N | R, \mathcal{H}_0)}, \end{aligned} \quad (5)$$

where we have used the law of conditional probability in the second equality; and in the third equality we used the fact that the probability distribution of R is insensitive to which hypothesis is valid. We use the following definition of the discrete Fourier transform (DFT) of an $m \times m$ pixel image $f[x, y]$

$$\mathcal{F}[f] = \hat{f}[k_x, k_y] = \sum_{x=0}^{m-1} \sum_{y=0}^{m-1} f[x, y] \exp\left(-2\pi i \frac{\vec{k} \cdot \vec{q}}{m}\right). \quad (6)$$

Here the hat sign marks the Fourier transform operator, the dot sign indicates the dot product, m is the image size, and $\vec{k} \equiv (k_x, k_y)$ are the frequency coordinates. Taking the Fourier transform of R and N (applying the convolution theorem)

$$\hat{R} = \left(\hat{T} + \alpha_r \hat{\delta}_{\vec{q}}\right) \hat{P}_r + \hat{\epsilon}_r, \quad (7)$$

$$\hat{N} = \left(\hat{T} + \alpha_n \hat{\delta}_{\vec{p}}\right) \hat{P}_n + \hat{\epsilon}_n. \quad (8)$$

Eliminating \hat{T} between Equations 7 and 8 we obtain

$$\hat{N} = \left[\frac{\hat{R} - \hat{\epsilon}_r}{\hat{P}_r} + \left(\alpha_n \hat{\delta}_{\vec{p}} - \alpha_r \hat{\delta}_{\vec{q}}\right) \right] \hat{P}_n + \hat{\epsilon}_n. \quad (9)$$

We now use the fact that the DFT of an $m \times m$ zero mean Gaussian noise image with i.i.d. pixels each with variance σ^2 , is a complex valued $m \times m$ random variable with i.i.d. real and imaginary frequency coefficients each with variance $m^2 \sigma^2 / 2$. We can therefore express the log-likelihood (up to a constant term which does not depend

¹¹ The Neyman-Pearson lemma states that the likelihood ratio test is the most powerful method for testing a simple hypothesis against an alternative.

¹² As shown later, our hypothesis can be regarded as a simple hypothesis.

on the data) of the new frequency-image conditioned on the reference image under \mathcal{H}_0 as

$$\begin{aligned} \log P(\hat{N} | \hat{R}, \mathcal{H}_0) &= - \sum_{k_x, k_y} \frac{|\hat{N} - \hat{R} \hat{P}_n / \hat{P}_r|^2}{2 \text{Var}(\hat{\epsilon}_n + \hat{\epsilon}_r \hat{P}_n / \hat{P}_r)} \\ &= - \frac{1}{2m^2} \sum_{k_x, k_y} \frac{|\hat{P}_r \hat{N} - \hat{P}_n \hat{R}|^2}{|\hat{P}_r|^2 \sigma_n^2 + |\hat{P}_n|^2 \sigma_r^2} \equiv LL_0, \end{aligned} \quad (10)$$

where the second line can be obtained from the first line by multiplying the numerator and denominator by $|\hat{P}_r|^2$ and using the definition of the variances of the noise terms $\hat{\epsilon}_r$ and $\hat{\epsilon}_n$.

In a similar fashion, for the alternative \mathcal{H}_1 and setting $\alpha \equiv \alpha_r = \alpha_n$, we obtain

$$\begin{aligned} \log P(\hat{N} | \hat{R}, \mathcal{H}_1) &= \\ - \frac{1}{2m^2} \sum_{k_x, k_y} \frac{|\hat{P}_r \hat{N} - \hat{P}_n \hat{R} + \alpha \hat{P}_n \hat{P}_r (\hat{\delta}_{\vec{q}} - \hat{\delta}_{\vec{p}})|^2}{|\hat{P}_r|^2 \sigma_n^2 + |\hat{P}_n|^2 \sigma_r^2} &\equiv LL_1. \end{aligned} \quad (11)$$

Writing $a \equiv \hat{P}_r \hat{N} - \hat{P}_n \hat{R}$ and $b \equiv \alpha \hat{P}_n \hat{P}_r (\hat{\delta}_{\vec{q}} - \hat{\delta}_{\vec{p}})$ we can express the log-likelihood-ratio (up-to a constant) as follows

$$LLR = LL_1 - LL_0 = - \frac{1}{2m^2} \sum_{k_x, k_y} \frac{|b|^2 + 2\Re[a\bar{b}]}{|\hat{P}_r|^2 \sigma_n^2 + |\hat{P}_n|^2 \sigma_r^2}, \quad (12)$$

where the $|b|^2$ term can be dropped because it does not depend on the observations. Here, \Re represents the real-part function, and the bar sign above a variable indicates the complex-conjugate operator. If the bar comes above the hat sign it means that the complex conjugate operator follows the Fourier transform. Defining the translation vector $\vec{\Delta} \equiv \vec{p} - \vec{q}$, and the center position \vec{x}_c between point source positions \vec{p} and \vec{q} to be $\vec{x}_c \equiv (x_c, y_c) \equiv \frac{\vec{p} + \vec{q}}{2}$, we obtain

$$\begin{aligned} \hat{\delta}_{\vec{q}} - \hat{\delta}_{\vec{p}} &= e^{-2\pi i \vec{k} \cdot \vec{q} / m} - e^{-2\pi i \vec{k} \cdot \vec{p} / m} \\ &= e^{-2\pi i \vec{k} \cdot \vec{x}_c / m} \left(e^{2\pi i \vec{k} \cdot \vec{\Delta} / 2m} - e^{-2\pi i \vec{k} \cdot \vec{\Delta} / 2m} \right) \\ &\approx e^{-2\pi i \vec{k} \cdot \vec{x}_c / m} \left[\left(1 + \frac{\pi i \vec{k} \cdot \vec{\Delta}}{m} \right) - \left(1 - \frac{\pi i \vec{k} \cdot \vec{\Delta}}{m} \right) \right] \\ &= \frac{2\pi i \vec{k} \cdot \vec{\Delta}}{m} e^{-2\pi i \vec{k} \cdot \vec{x}_c / m}, \end{aligned} \quad (13)$$

where the approximation between the second and third lines holds for sufficiently small translations where we may keep only terms first order in $\vec{k} \cdot \vec{\Delta}$.

Using the fact that $|b|^2 = \mathcal{O}((\vec{k} \cdot \vec{\Delta})^2)$, we find

$$\begin{aligned} \Re[a\bar{b}] &\approx \\ \frac{2\pi \alpha \vec{k} \cdot \vec{\Delta}}{m} \Im \left[\hat{P}_n \hat{P}_r (\hat{P}_r \hat{N} - \hat{P}_n \hat{R}) e^{2\pi i \vec{k} \cdot \vec{x}_c / m} \right], &\end{aligned} \quad (14)$$

where the \Im function is the imaginary-part function that replaces the \Re function due to multiplication by the imaginary unit i . Substituting the above into the ex-

pression for the LLR (Equation 12) we find that

$$LLR \approx -\frac{1}{2m^2} \sum_{k_x, k_y} \frac{2\Re[a\bar{b}]}{|\hat{P}_r|^2\sigma_n^2 + |\hat{P}_n|^2\sigma_r^2} = \quad (15)$$

$$\alpha\vec{\Delta} \cdot \Im \left\{ \frac{1}{2m^2} \sum_{k_x, k_y} \left[\frac{4\pi\vec{k} \cdot \hat{P}_n \hat{P}_r (\hat{P}_n \hat{R} - \hat{P}_r \hat{N})}{m |\hat{P}_r|^2\sigma_n^2 + |\hat{P}_n|^2\sigma_r^2} e^{2\pi i \vec{k} \cdot \vec{x}_c / m} \right] \right\}.$$

Defining the following two component frequency image (one component for each spatial frequency direction)

$$\vec{\tilde{z}} \equiv \frac{4\pi\vec{k} \cdot \hat{P}_n \hat{P}_r (\hat{P}_n \hat{R} - \hat{P}_r \hat{N})}{m |\hat{P}_r|^2\sigma_n^2 + |\hat{P}_n|^2\sigma_r^2}, \quad (16)$$

and identifying the inverse DFT, with respect to the image coordinate \vec{x}_c , in the last expression for the LLR , we define

$$\vec{z} \equiv \mathcal{F}^{-1} \left[\vec{\tilde{z}} \right], \quad (17)$$

and find (to first order in $\vec{k} \cdot \vec{\Delta}$) that

$$LLR(q; \alpha\vec{\Delta}) \approx \alpha\vec{\Delta} \cdot \Im \left\{ \mathcal{F}^{-1} \left[\vec{\tilde{z}} \right] \right\} \quad (18)$$

$$= \alpha\vec{\Delta} \cdot \text{Im}[\vec{z}] = \alpha\Delta \left(\vec{\Delta}_u \cdot \text{Im}[\vec{z}] \right),$$

where we use the symbol $\vec{\Delta}_u \equiv \frac{\vec{\Delta}}{\|\vec{\Delta}\|}$ to denote the unit vector in the direction of the translation of $\vec{\Delta}$.

Then, according to the Neyman-Pearson lemma, rejecting \mathcal{H}_0 when $\vec{\Delta}_u \cdot \Im[\vec{z}] > \eta$, for some threshold η , is the most powerful test at significance level $P(\vec{\Delta}_u \cdot \Im[\vec{z}] > \eta | \mathcal{H}_0)$. This assumes that the direction of translation, $\vec{\Delta}_u$ is known. We generalize this in the following section.

2.3. Detecting pure motion for any translation

To find a statistic that is most powerful at a certain significance level for any direction of translation, we modify the alternative hypothesis of the previous section to the following

$$\tilde{\mathcal{H}}_1 : \|\vec{q} - \vec{p}\| = \Delta. \quad (19)$$

This leads to the following likelihood ratio:

$$LR(q; \Delta, \alpha) = \frac{P(N, R | \tilde{\mathcal{H}}_1)}{P(N, R | \mathcal{H}_0)}. \quad (20)$$

Defining θ to be the angle between $\vec{\Delta}_u$ and the positive x -axis in the image plane, then

$$LR(q; \Delta, \alpha) = \int_0^{2\pi} d\theta \exp\left(LLR(q; \alpha\vec{\Delta}) \right) \quad (21)$$

$$= \int_0^{2\pi} d\theta' \exp\left(\alpha\Delta (\cos\theta' \|\Im[\vec{z}]\|) \right),$$

which, for any positive value of $\alpha\Delta$, is an increasing function of $\|\Im[\vec{z}]\|$ (this can be shown using the fact that for every $r > 0$, $\frac{d}{dr} [\exp(r) + \exp(-r)] = \exp(r) - \exp(-r) > 0$).

We thus conclude that a threshold test of the statistic

$$Z^2(x, y) \equiv \|\Im[\vec{z}]\|^2 \quad (22)$$

$$= \left\| \Im \left\{ \mathcal{F}^{-1} \left[\frac{4\pi\vec{k} \cdot \hat{P}_n \hat{P}_r (\hat{P}_n \hat{R} - \hat{P}_r \hat{N})}{m |\hat{P}_r|^2\sigma_n^2 + |\hat{P}_n|^2\sigma_r^2} \right] \right\} \right\|^2,$$

is a most powerful test, at a specific significance level, for detecting a point source, having a center pixel coordinates $(x, y) \equiv \vec{x}_c \equiv (\vec{p} + \vec{q})/2$ undergoing a translation in *any* direction. We call this last expression the *transient statistic* (Z^2). An important property of Equation 22 is that it is anti-symmetric¹³ and numerically stable¹⁴ (i.e., no division by zero). Given the definition of Z^2 , its values are distributed like the χ^2 distribution with two degrees of freedom.

2.4. Distinguishing motion from flux variation

Given a transient detection, we would like to know what the likely cause of the transient detection is: a motion of a point source or a change in its flux.

In the case that we are interested only in knowing which model (flux variation or motion) better explains the residuals, we can compare the transient statistic Z^2 (Equation 22) against the proper subtraction statistic S , where S is defined in Equations (A26) and (A27) of Zackay et al. (2016). As the two statistics are strictly not produced by nested models, the comparison has to occur indirectly. We use two equivalent methods: (i) to convert the Z^2 to Gaussian significance (assuming χ^2 distribution with two degrees of freedom) – we call this significance Z_σ , and to compare it with $|S|$; (ii) Since S follows a normal distribution, S^2 is distributed like a χ^2 distribution with one degree of freedom. Therefore, we can compare $S^2 + 1$ to Z^2 .

We note that before using S^2 and Z^2 (or S and Z_σ), it is recommended to normalize them empirically, such that S will have a mean (or median) of zero and a standard deviation (or robust standard deviation) of 1. Similarly, S^2 and Z^2 can be normalized such that their mean, median, or variance, will be k , $k(1 - 2/(9k))^3$, or $\sqrt{2k}$, respectively, where k is the number of degrees of freedom. Finally, if $Z^2 > S^2 + 1$ (or $Z_\sigma > |S|$), then the motion model is preferred, while if $Z^2 < S^2 + 1$, then the variability model is more likely.

An important implementation comment is that, as seen in Figure 2, the local maxima in $|S|$ and Z_σ are not at the same location. Therefore, our recommendation for implementation is as follows: (i) Look for a local maximum in $|S|$ that is larger than the detection threshold (e.g., 5σ); (ii) For each local maximum in $|S|$, look for the maximum value of Z_σ within a radius of X pixels from the local maximum position in $|S|$; (iii) If $|S| > Z_\sigma$, then declare that the local maximum is a transient candidate. In our own implementation which is described below, we used a radius of $X = 5$ pix (about 2–2.5 times the FWHM). When we compare $|S|$ and Z_σ , we always refer to the maximum of Z_σ found near the local maximum of $|S|$.

¹³ Meaning that one can switch the role of R and N and this will return the same result with opposite sign.

¹⁴ The numerator converges to zero faster than the denominator.

2.5. Fitting motion and flux variation

Another approach is to fit a model that mixes flux variations and motion, and therefore allows one to consider more complicated cases, in which the transient is both moving and variable. To do so, we use the new and reference image models defined in equations 1 and 2, where we now allow for observed flux variation, so that α_r will generally differ from α_n . Using the definitions of the Fourier transforms of the reference image \hat{R} and the new image \hat{N} (equations 7 and 8), we may eliminate \hat{T} by writing

$$\hat{P}_r \hat{N} - \hat{P}_n \hat{R} = \hat{P}_n \hat{P}_r (\alpha_n \hat{\delta}_{\vec{p}} - \alpha_r \hat{\delta}_{\vec{q}}) + \hat{P}_r \hat{\epsilon}_n - \hat{P}_n \hat{\epsilon}_r. \quad (23)$$

This motivates the introduction of the following frequency domain difference image:

$$\begin{aligned} \hat{D}_T &\equiv \hat{P}_r \hat{N} - \hat{P}_n \hat{R} + \hat{P}_n \hat{P}_r (\alpha_r \hat{\delta}_{\vec{q}} - \alpha_n \hat{\delta}_{\vec{p}}) \\ &= \hat{P}_r \hat{\epsilon}_n - \hat{P}_n \hat{\epsilon}_r. \end{aligned} \quad (24)$$

Here, we get the second line by using equations 2 and 1. In Appendix A we show that this specific choice of a difference image \hat{D}_T captures all the available information (from the observed R and N) for the purpose of finding the model parameters α_r , α_n , \vec{q} , and \vec{p} . In other words, that \hat{D}_T is a *sufficient statistic*¹⁵ with respect to the model parameters.

We now express the log-likelihood of observing \hat{D}_T for a given α_r , α_n , \vec{q} and $\vec{p} = \vec{q} + \vec{\Delta}$ as

$$\begin{aligned} \log P(\hat{D}_T | \alpha_r, \alpha_n, \vec{q}, \vec{p}) &= -\log \zeta \\ &- \frac{1}{2m^2} \sum_{k_x, k_y} \frac{|\hat{P}_r \hat{N} - \hat{P}_n \hat{R} + \hat{P}_n \hat{P}_r (\alpha_r \hat{\delta}_{\vec{q}} - \alpha_n \hat{\delta}_{\vec{p}})|^2}{|\hat{P}_r|^2 \sigma_n^2 + |\hat{P}_n|^2 \sigma_r^2}, \end{aligned} \quad (25)$$

where we have included the Gaussian normalization term

$$\log \zeta \equiv \frac{1}{2} \sum_{k_x, k_y} \log \left[2\pi m^2 \left(|\hat{P}_r|^2 \sigma_n^2 + |\hat{P}_n|^2 \sigma_r^2 \right) \right]. \quad (26)$$

We can specialize Equation 25 to the small translation limit by keeping only terms first order in $\vec{k} \cdot \vec{\Delta}$. This can be achieved by substituting:

$$\begin{aligned} \alpha_r \hat{\delta}_{\vec{q}} - \alpha_n \hat{\delta}_{\vec{p}} &= \alpha_r e^{-2\pi i \frac{\vec{k} \cdot \vec{q}}{m}} - \alpha_n e^{-2\pi i \frac{\vec{k} \cdot \vec{p}}{m}} \\ &= e^{-2\pi i \vec{k} \cdot \frac{\vec{q} + \vec{p}}{2m}} \left(\alpha_r e^{2\pi i \vec{k} \cdot \frac{\vec{\Delta}}{2m}} - \alpha_n e^{-2\pi i \vec{k} \cdot \frac{\vec{\Delta}}{2m}} \right) \\ &\approx e^{-2\pi i \frac{\vec{k} \cdot \vec{x}_c}{m}} \left[(\alpha_r - \alpha_n) + (\alpha_r + \alpha_n) \frac{\pi i (\vec{k} \cdot \vec{\Delta})}{m} \right], \end{aligned} \quad (27)$$

where we again use the image coordinate $\vec{x}_c \equiv \frac{\vec{q} + \vec{p}}{2}$. In this limit, a set of independent parameters for the likelihood are the flux difference $(\alpha_r - \alpha_n)$, the flux sum multiplied by the magnitude of translation $(\alpha_r + \alpha_n) \|\Delta\|$ and the angle θ between the direction of translation $\vec{\Delta}_u$ and the positive direction of the x -axis.

¹⁵ In statistics, a statistic is sufficient with respect to a statistical model and its associated unknown parameter if no other statistic that can be calculated from the same sample provides any additional information as to the value of the parameter.

We also write Equation 25 using the following two alternative parametrizations (which we will find useful in §3.2):

$$\log P(\hat{D}_T | \alpha_r, \alpha_n, \vec{\Delta}, \vec{x}_c) = \quad (28)$$

$$\log P(\hat{D}_T | \alpha_r - \alpha_n, \alpha_r + \alpha_n, \|\Delta\|, \theta, \vec{x}_c) = \quad (29)$$

$$\log P(\hat{D}_T | \alpha_r, \alpha_n, \vec{q}, \vec{p}),$$

and we denote the linearized version of Equation 25 where we substitute the above approximation for $\alpha_r \hat{\delta}_{\vec{q}} - \alpha_n \hat{\delta}_{\vec{p}}$ (the left hand side of Equation 28) as

$$\log P(\hat{D}_T | \alpha_r - \alpha_n, (\alpha_r + \alpha_n) \|\Delta\|, \theta) = \quad (30)$$

$$\log P(\hat{D}_T | \alpha_r, \alpha_n, \vec{q}, \vec{p}) + \mathcal{O}(\|\vec{\Delta}\|^2)$$

The importance of D_T is that it can be used to fit α_r , α_n , $\vec{\Delta}$, \vec{x}_c , simultaneously (see §3.2).

A disadvantage of this approach over the test suggested in §2.4 is that if the source flux is constant, fitting the full model will result in lower sensitivity, compared to employment of Z^2 . Furthermore, fitting the likelihood in Equation 30 is computationally expensive. Therefore, we suggest using this approach only in the rare cases when both flux variations and motion are suspected.

3. SIMULATIONS

In this section, we demonstrate the operation and measure the performance of the transient statistic $Z^2(x, y)$ (Equation 22), as well as of the difference image likelihood function $\log P(\hat{D}_T | \alpha_r, \alpha_n, \vec{q}, \vec{p})$ (Equation 25). Specifically, we measure the performance of $Z^2(x, y)$ as a detector of pure motion in §3.1 and the ability of $\log P(\hat{D}_T | \alpha_r, \alpha_n, \vec{q}, \vec{p})$ to distinguish between motion and flux variation in §3.2.

The performance of the new algorithm is shown on simulated 64×64 pixel image pairs, $R(x, y)$ and $N(x, y)$, the synthetic reference, and new images, respectively. These images simulate the generative process of equations 1 and 2 assuming a static true background image (setting $T = 0$). Image pairs are generated using 2-D Gaussian profile point spread functions $P_r(x, y)$ and $P_n(x, y)$ having various aspect ratios and orientations (defined below). To generate R and N with sub-pixel point source positions \vec{q} and \vec{p} we first evaluate the (continuous) 2-D Gaussian profiles used to generate P_r and P_n at sub-pixel offsets and then add zero mean per pixel Gaussian noise with variances σ_r^2 and σ_n^2 respectively. In Figure 1 we show an example of one such image pair.

3.1. Performance evaluation of the transient detector

We now test the performance of the *transient* statistic and compare it to the *proper image subtraction* statistic. Proper image subtraction was designed to be an optimal detector of a general local change in flux and does not assume that the transient is due to a translating point source. We thus expect that the optimality of the transient statistic in this specific translational data generation process would lead to enhanced detector performance. For this purpose, we generate a set of six simulations having varying background noise levels (simulations 1-3) and translation sizes (simulations 4-6). The

TABLE 1
PARAMETERS COMMON TO DETECTOR PERFORMANCE
SIMULATIONS

α_r	α_n	W_r (pix)	W_n (pix)	H_r (pix)	H_n (pix)	β_r (deg)	β_n (deg)
2.5	2.5	5.0	5.0	3.0	3.0	90	0

NOTE. — Here α_r (α_n) is the flux level of the point source in the reference (new) image, W_r and H_r (W_n and H_n) are the Gaussian profile width and height parameters of the reference (new) image PSF in pixels and β_r (β_n) is the orientation angle of the PSF in the reference (new) image.

TABLE 2
NOISE AND TRANSLATION LEVELS IN
DETECTOR PERFORMANCE SIMULATIONS

Simulation	σ_r	σ_n	Δ_x (pix)	Δ_y (pix)
1	0.002	0.002	1.0	1.0
2	0.003	0.003	1.0	1.0
3	0.004	0.004	1.0	1.0
4	0.003	0.003	1.4	1.4
5	0.003	0.003	1.1	1.1
6	0.003	0.003	0.8	0.8

NOTE. — Here for each simulation, σ_r (σ_n) is the standard deviation value of the per-pixel additive white Gaussian flux noise in the reference (new) image R (N), measured in the α_r (α_n) arbitrary flux units. The components of the translation vector (Δ_x, Δ_y) $\equiv \bar{\Delta} \equiv \bar{p} - \bar{q}$ between the position of the point source in the reference and new images, are in the units of pixels. Simulations 1-3 vary the flux noise at constant translation and simulations 4-6 vary the length of the translation vector at constant noise levels.

full set of parameters used in these simulations is summarized in Tables 1 and 2. In each simulation, two sets of 10^4 image pairs were generated – one set was of positive examples that did contain a translating point source (such as the pair shown in Figure 1) and the other set was of negative examples which contained only background noise.

For each image pair, we computed the transient statistic image $Z^2(x, y)$ as well as the (squared) proper statistic image $S^2(x, y)$. We show in Figure 2 an example of these transient and proper statistic images evaluated on the positive example of Figure 1. We typically see that the center position of the sources coincides with the position of the peak in $Z^2(x, y)$ while in $S^2(x, y)$ a double peak (on both sides of the source center position) is visible. In Figure 3 we show an example of the two image statistics when they are evaluated on a negative example pair. These patterns, resulting from the background noise, are eventually responsible for the false positive detection events of each of these detectors (note that the contrast in Figure 3 was enhanced by a factor of ~ 5 compared to that of Figure 2).

To quantitatively compare the performance of each image statistic as a detector of pure translation we compute for each simulation and for each image statistic

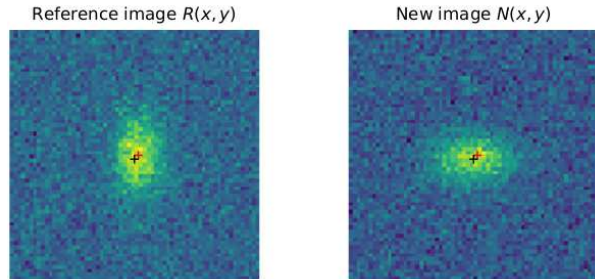


FIG. 1.— Example of a pair of reference and new images generated in simulation 1 (see Table 2). The red and black crosses mark the positions of the original point sources in the reference and new images respectively. It can be seen that the translation is a one-pixel translation (diagonally), which is considerably smaller than the width of the PSFs and that the Gaussian PSF profile of the new image differs from that of the reference image by a 90° rotation.

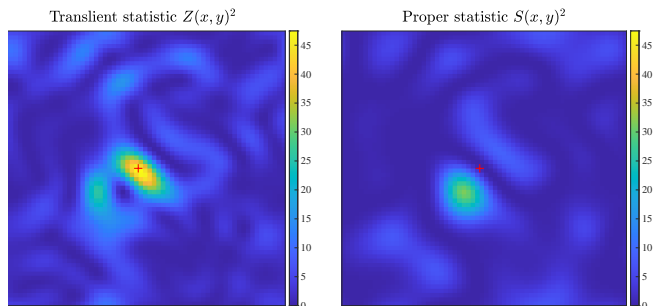


FIG. 2.— Resulting *transient statistic* (Z^2 ; left panel) and *proper statistic* (S^2 ; right panel) images computed for the image pair shown in Figure 1. The red crosses mark the location of $\bar{x}_c \equiv (\bar{p} + \bar{q})/2$, the center between the positions of the point sources in the reference and new images. In the squared *transient statistic* image one can see a single peak approximately centered at \bar{x}_c whereas in the squared *proper statistic* image two peaks on opposite sides of \bar{x}_c (diagonally) can be observed. This is the typical qualitative appearance of the two detector images when the data is generated by a point source undergoing pure translation (without any flux change).

(transient and proper) a curve showing the relative rates of the true positive detection as a function of the false positive detection rates (known as a receiver operating characteristic [ROC] curve). We define the true positive detection rate of each detector (above some threshold) to be the number of positive examples that were detected as such, divided by the total number of positive examples in the simulation. Similarly, the false positive rate is the number of negative examples that the detector incorrectly classified as positive examples divided by the total number of negative examples.

For a given threshold level, we define each detector's response to be positive if at least one pixel in the statistic image was above this threshold. We show the resulting curves for simulations 1-3 in Figure 4 (where the noise level was varied), and for simulations 4-6 in Figure 5 (where the translation length was varied). One can see, that for all simulations and at all values of the false-positive rate, that the transient statistic detector achieves a higher true-positive detection rate compared to that of the proper statistic detector. One can also see that lower levels of noise and larger translations allow

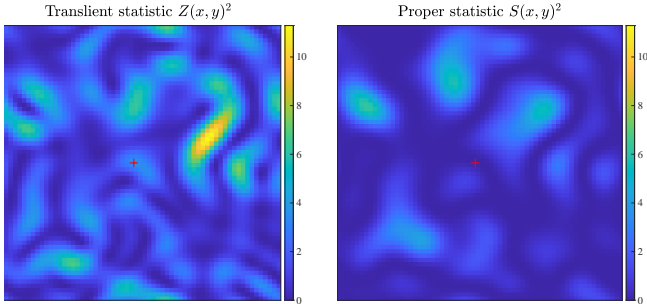


FIG. 3.— Resulting *transient statistic* (Z^2 ; left panel) and *proper statistic* (S^2 ; right panel) images computed for zero-mean noise-only images (no moving point source). These patterns (arising from the action of the *transient statistic* and *proper statistic* on the observational noise) are responsible for false-positive detection events (at a certain detection threshold), i.e., cases of an event being classified as a detection of a translating point source when there was none. The highest peak, on the left panel, ($Z^2 \cong 11$) corresponds to a false alarm probability of 0.004 per pixel (i.e., χ^2 distribution with two degrees of freedom), and close to unity for 64^2 trials.

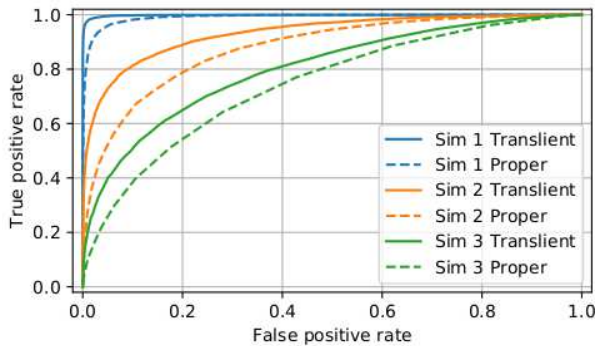


FIG. 4.— Receiver operating characteristic curve (ROC curve) for simulations 1-3 (varying levels of flux noise) showing the rates of true-positive events as a function of the false-positive event rate. These curves were generated by varying detector threshold levels η over an appropriately wide range. Each color represents a simulation index (noise level) while solid (dashed) curves represent the resulting performance when using the *transient statistic* (*proper statistic*). One can see that for all simulations and at all values of the false-positive rate, the *transient statistic* achieves a higher true-positive detection rate compared to the *proper statistic*. We also see that lower levels of noise allow the detectors to reach higher true-positive rates at set false-positive rates.

both detectors to reach higher true-positive rates for a given set of false-positive rates.

3.2. Performance evaluation of fitting for motion and flux variation simultaneously

In some rare cases, one may want to check the possibility that the source is both moving and variable. For this purpose in §2.5 we derived expressions for the likelihood of observing the difference image D_T due to a point source centered at \vec{x}_c that has translated $\vec{\Delta}$ pixels and changed flux from α_r in the reference image to α_n in the new image (Equations 28, 29 and 30). In this section, we use simulations 7 and 8, where both the flux and the position of the point source change, and evaluate the likelihood of these observations. The full set of parameters of simulations 7 and 8 is provided in Table 3. Simulation

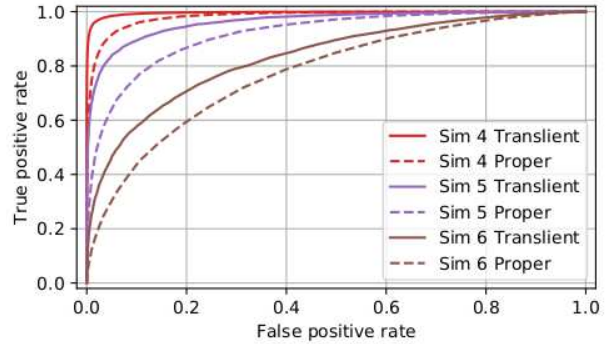


FIG. 5.— ROC curves similar to Figure 4 but for simulations 4-6.

7 differs from simulation 8 such that in simulation 7 the translation is larger than the size of the PSF, whereas in simulation 8 the translation is marginally smaller. To evaluate the likelihood functions in this section we perform Markov chain Monte Carlo (MCMC) sampling using the EMCEE package (Foreman-Mackey et al. 2013) by randomly initializing 100 chains near the parameter origin and running each chain through 100 warm-up iterations and an additional 650 sampling iterations.

We show in Figure 6 the resulting MCMC sample distribution of the likelihood function $P(\hat{D}_T | \alpha_r, \alpha_n, \Delta_x, \Delta_y)$ (Equation 28, after setting the point source center position \vec{x}_c to its true simulated value), when evaluated on simulation 7. In the case of simulation 7, where the point source is well separated between the reference and new images (compared to the PSF widths), one can see that the model parameters $\Delta_x, \Delta_y, \alpha_r, \alpha_n$ are non-degenerate, and that the resulting sample distribution may be used to distinguish between a change in flux and a translation of the point source.

In Figure 7 we show the resulting MCMC sample distribution for simulation 8, where the convolved point sources of the reference and new images are not well separated. One can see that in this case when using model parameters $\Delta_x, \Delta_y, \alpha_r, \alpha_n$, there is a strong dependence (or approximate degeneracy) between these parameters. Such a dependence hampers the ability to distinguish between a change in flux and a translation of the point source.

To partially deal with this degeneracy, one can switch to a new set of (more orthogonal) parameters: $\|\Delta\|, \theta, \alpha_r - \alpha_n$ and $\alpha_r + \alpha_n$. In Figure 8 we present the result of sampling the same distribution (for simulation 8), but with this new set of parameters. One can see that this change of variables largely decouples most (but not all) of the parameters, leaving a clear dependence between $\|\Delta\|$ and $\alpha_r + \alpha_n$.

Finally, we show in Figure 9 the result of sampling the linearized likelihood (Equation 30), again for the “small translation” simulation 8. The linearized likelihood depends only on the three parameters $\alpha_r - \alpha_n, (\alpha_r + \alpha_n)\|\Delta\|$ and θ (after setting \vec{x}_c to its true simulated value). One can see that when using this reduced set of model parameters, the likelihood does not show a strong dependence between the parameters. To summarize, in some circumstances, inference using this set of model parameters can allow us to distinguish motion

TABLE 3
PARAMETERS USED IN THE MOTION VS. FLUX-VARIATION
SIMULATIONS

Simulation	α_r	α_n	σ_r	σ_n	H,W (pix)	Δ_x (pix)	Δ_y (pix)
7	2	3	0.0025	0.0025	4.0	12	0
8	2	3	0.0025	0.0025	4.0	2	0

NOTE. — Parameters of the additional simulations discussed in §3.2 to study the ability to distinguish between point source motion and point source flux variation. The columns are similar to those of Tables 1 and 2 while here H and W denote the equal horizontal and vertical Gaussian profile diameter of the reference and the PSFs of the new image. In both simulations all the parameters other than the translation length are equal. In these two simulations, both the flux and the point source position are changed between the reference and new images. In simulation 7 the motion is larger than the PSF resolving diameter, while in simulation 8 it is marginally smaller than the PSF.

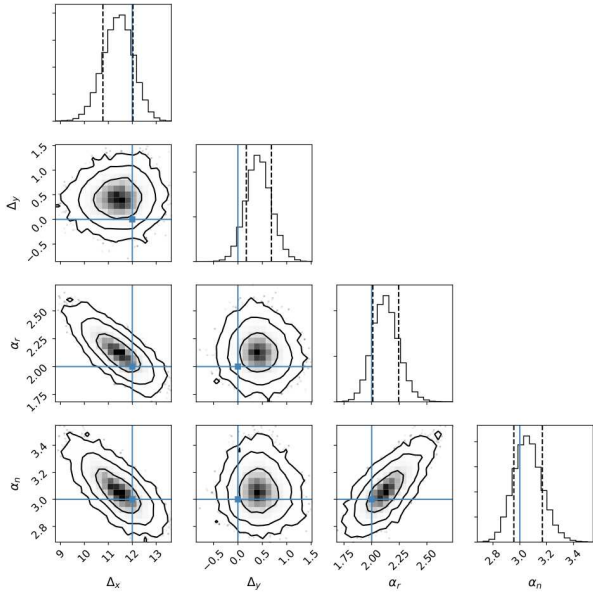


FIG. 6.— The likelihood function $P(\hat{D}_T | \Delta_x, \Delta_y, \alpha_r, \alpha_n)$ evaluated for simulation 7 using the (true) point source center location $\vec{x}_c = (\vec{p} + \vec{q})/2$ as a function of model parameters Δ_x , Δ_y , α_r , α_n (see §2.4). The evaluation was performed using Markov chain Monte Carlo sampling. The figure shows the marginal distributions over single parameters (upper diagonal) as well as the marginal distributions for all parameter pairs (off-diagonal). The blue point indicates the true model parameters while the curves indicate the 68%, 95% and 99.7% confidence regions. The dashed vertical lines indicate the 1-sigma confidence intervals in the 1-D marginals.

and flux variation when the translations are smaller than the PSF.

4. TESTS ON REAL ASTRONOMICAL IMAGES

To test the performance of the transient statistic Z^2 (Equation 22) on real astronomical data we have used images obtained with the Large Array Survey Telescope (LAST; Ofek et al. 2023a; Ben-Ami et al. 2023). These images have been taken over the course of one night on 2023 Apr 25 from the LAST site at Neot Smadar, Israel. The data was reduced using the LAST pipeline (Ofek 2014; Soumagnac and Ofek 2018; Ofek 2019; Ofek et al. 2023b).

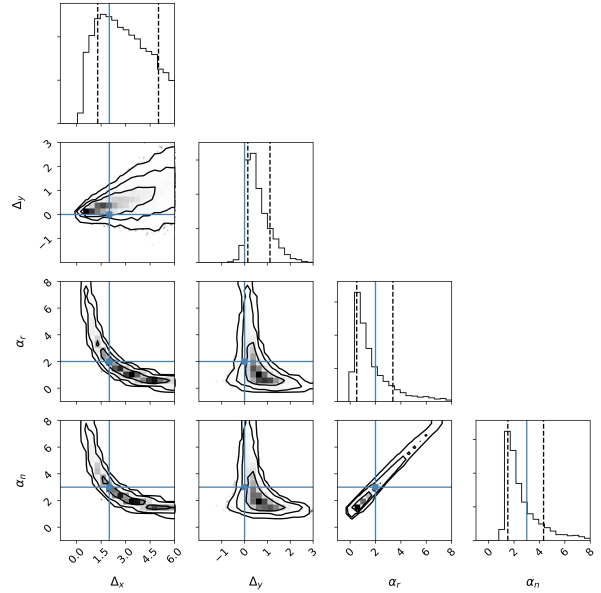


FIG. 7.— The likelihood function $P(\hat{D}_T | \Delta_x, \Delta_y, \alpha_r, \alpha_n)$, similar to Figure 6 but evaluated for simulation 8 where the translation length is smaller than the resolving width of the PSFs.

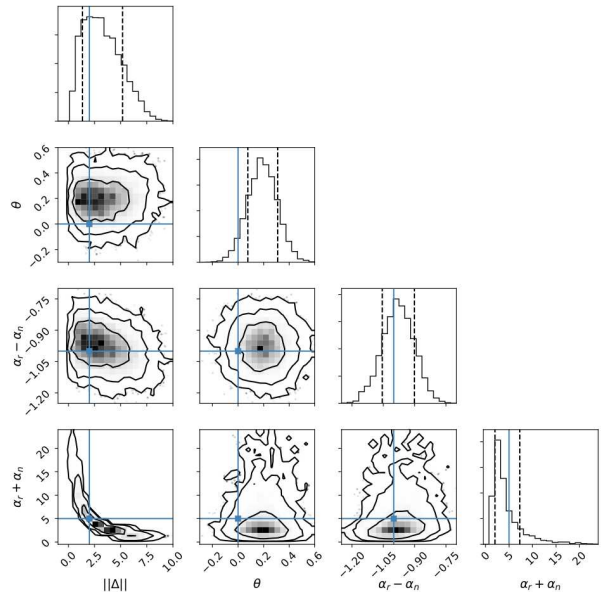


FIG. 8.— The likelihood function $P(\hat{D}_T | \|\Delta\|, \theta, \alpha_r - \alpha_n, \alpha_r + \alpha_n)$, similar to Figure 7 and similarly evaluated for simulation 8 (where the translation is small compared to the PSF) but using a different set of variables to display the same distribution. One can see that this change of variables largely decouples most (though not all) of the parameters, leaving a clear dependence between $\|\Delta\|$ and $\alpha_r + \alpha_n$.

One of the most important applications of Z^2 is to distinguish between flux-variation and motion of a source. To test this capability, we derived Z_σ and $|S|$ on consecutive images of a stationary variable source, and of a moving non-variable source. As explained in §2.4, we first looked for local maxima in $|S|$, and then chose the maximum of Z_σ within 5 pixels from the local maximum of $|S|$.

For the variable source, we analyzed images captur-

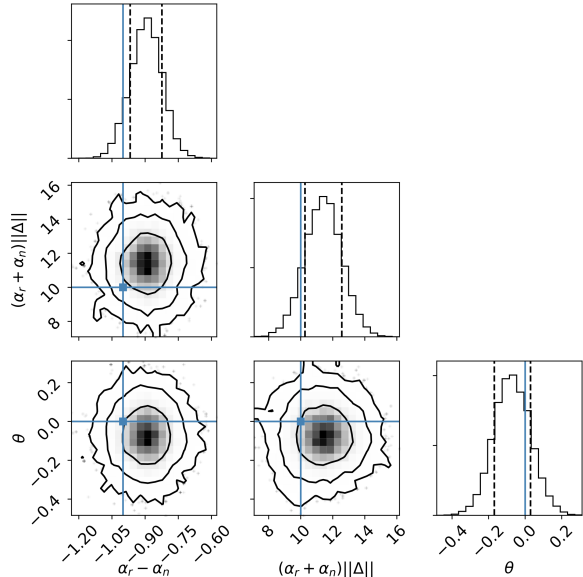


FIG. 9.— The likelihood function $P(\hat{D}_T | \alpha_r - \alpha_n, (\alpha_r + \alpha_n) \|\Delta\|, \theta)$, obtained by linearizing Equation 25 in $\vec{k} \cdot \vec{\Delta}$. Here, evaluation is again for the small translation simulation 8 (as in Figures 7 and 8). One can see that this reduced set of model parameters (in the linearized likelihood) does not show a strong dependence and may therefore be preferable in the small translation limit.

ing LINEAR 3506385, an eclipsing binary with a period of ≈ 0.22 d and an average V-band magnitude of 15.96 (Drake et al. 2014). In the selected data, the observations cover a brightening phase of the binary. We thus use one of the first images as the reference image and perform subtraction of subsequent images, registered to the reference image. The standard deviation in the astrometric solution of the binary’s Right Ascension and Declination coordinates within the data is about 80 mas. As the binary brightens over time, both statistics increase, whereas $|S|$ leads to overall higher significance than Z_σ (Figure 10). This result is consistent with the interpretation of a variable stationary source.

As a moving source example, we analyzed images capturing the asteroid 3832 (Shapiro). The asteroid’s motion between two successive images is about ≈ 0.3 arcsec, whereas the LAST pixel scale is 1.25 arcsec pix^{-1} . We used the first image as a reference image so that the time series of subsequent registered images represents a source moving further away from its initial position. Figure 11 shows $|S|$ and Z_σ as functions of the asteroid’s motion relative to the reference image. The results clearly show that for small translations, when the shift is smaller than the PSF size, Z_σ yields a larger significance than $|S|$. Once the asteroid has moved far enough to clearly separate it in the new image from itself in the reference image, it effectively becomes a transient, and $|S|$ overtakes Z_σ .

5. CODE

The transient algorithm was implemented both as Python and MATLAB codes. The Python code includes a core functionality that receives the new image, a reference image, and their PSFs. The new and reference images should be flux-matched and registered. The core

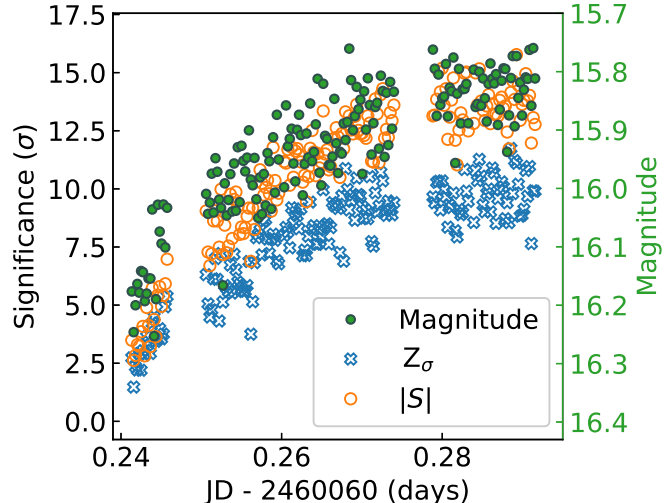


FIG. 10.— A comparison of Z_σ (blue empty X’s) and $|S|$ (orange empty circles) for a series of images capturing a variable star in the FoV. The measured LAST magnitude of the star (green solid circles) is also shown, with its value read on the right y-axis. For a stationary variable star, $|S|$ is dominant.

function returns \hat{z} data product. This function, along with the likelihood functions and code to generate the plots in this paper, are available from GitHub¹⁶.

The MATLAB code is available as part of the AstroPack/MAATv2 package available from GitHub¹⁷. The MATLAB code includes a core function¹⁸, a ZOGY plus TRANSLIENT class¹⁹, and many high-level functions that allow the construction of the PSF, registering the images, measure the zero points, apply proper subtraction, and more. The image subtraction utilities are also described, with examples, in the AstroPack live wiki page²⁰.

6. DISCUSSION

We have presented a novel extension to the work of Zackay et al. (2016) to detect and measure transients that result from a point source undergoing translation given a pair of temporally separated images of the event. For the case of a pure translation (no flux change), and when the translation is smaller than the PSF size, we derive an optimal statistic that can detect such transients for any, a priori unknown, direction of motion. We show, using simulated examples, that our derived statistic, when applied to moving sources, reaches a higher true-positive detection rate at all false-positive detection rates, compared to the *proper subtraction* statistic of Zackay et al. (2016). This is the case at various levels of background noise and for various small, compared to the PSF, non-zero translations.

When dealing with transient detection, this method should be used together with the proper image subtraction (ZOGY) method. While ZOGY is optimal for flux

¹⁶ <https://github.com/ofersp/translient>

¹⁷ <https://github.com/EranOfek/AstroPack>

¹⁸ Function name `imUtil.properSub.translient`

¹⁹ Implemented in the `AstroZOGY` class.

²⁰ <https://github.com/EranOfek/AstroPack/wiki/imProc.sub> and <https://github.com/EranOfek/AstroPack/wiki/AstroZOGY>

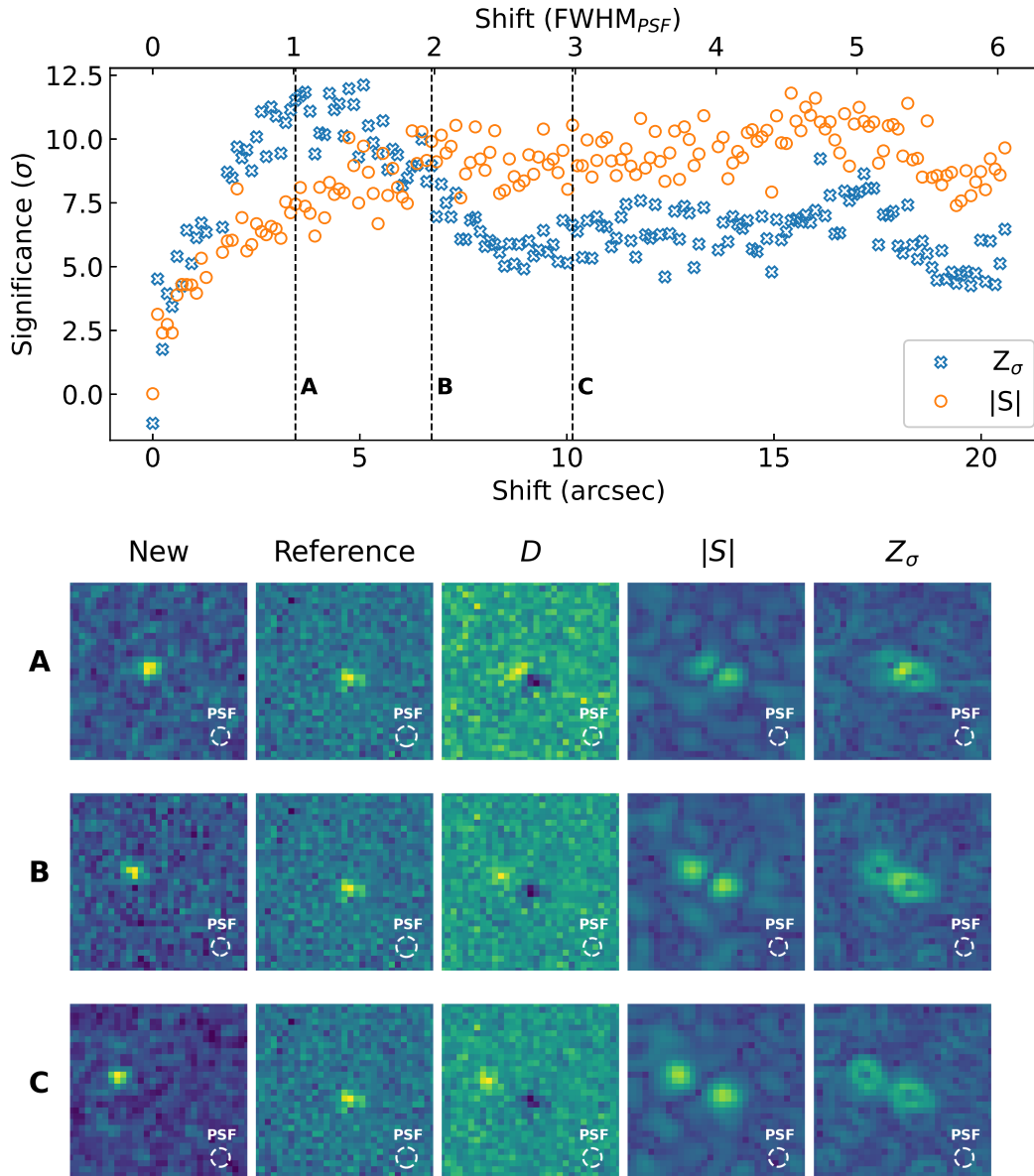


FIG. 11.— **Upper panel:** A comparison of Z_σ (blue empty X's) and $|S|$ (orange empty circles) for a series of images capturing a moving source (asteroid 3832 Shapiro). The images are taken sequentially within one hour during the same night. The first image serves as the reference image. Each sequential new image thus represents a source moving away from its initial position. The distance, that the asteroid has crossed since the time of the reference image, is shown as a shift in arcseconds and in the FWHM of P_r . Three selected measurements, where the shift is closest to a multiple of FWHM_{PSF} , are marked by gray dashed vertical lines and designated by the letters A, B, and C. **Lower panel:** For each of the three marked measurements (A, B, C), a set of cutouts of the new, reference, D , $|S|$, and Z_σ images around the initial asteroid position are shown. For the $|S|$ and Z_σ cutouts, the minimum and maximum values of the colormap are fixed to -5σ and 13σ , respectively. For each cutout, the dashed circle shows the FWHM of the PSF of the respective image. For $|S|$ and Z_σ , the shown PSF is that of the D image. Within a shift of $\lesssim 2 \text{FWHM}_{\text{PSF}}$, $Z_\sigma > |S|$. Once the asteroid positions in the reference and new images are clearly separated, $|S|$ overtakes Z_σ .

variation, TRANSLIENT is optimal for motion. Therefore, the combination of the two methods allows one to discern between variability (or transient detection) and motion (e.g., due to astrometric scintillation noise). Specifically, calculating both statistics and comparing their significance allows us to tell which model better explains the flux residuals in the subtraction image - is it variability or motion? We have demonstrated this capability using real telescope images of an asteroid and a variable source. We argue that this is a powerful statistic to distinguish between transients/variables and source motion due to

registration errors, scintillation noise, color-refraction, or astrophysical motion.

For the case where the transient detection results from both a change in position and a change in flux, we additionally derive the likelihood function for observing a particular difference image (shown to sufficiently capture all the necessary information) which is then used to disambiguate changes in flux and position. Using simulated examples, we have studied the behavior of this likelihood function, when the translation is either larger or smaller than the PSF diameter, and using three different param-

eterizations of the likelihood. We show that for large translations, this likelihood function can distinguish between motion and flux variation in all cases. For translations smaller than the PSF, a degeneracy (or strong dependence) of the parameters occurs in the likelihood in some of the parameterizations. Using a linearized version of the likelihood, we have found a reduced set of non-degenerate parameters which are preferable for discrimination between translation and flux variation in the case of small translations.

Our method is unique in that it enables the detection of translating point sources in crowded fields and on top of a complex background for which no good models exist. It is derived from a well-defined generative process, is essentially non-parametric, and is optimal in the case of small pure translations. Particular cases where the newly developed detector method may find use are (but not limited to): (i) reducing the amount of false alarms, due to motion, in a transient detection algorithm implementation; and (ii) measuring the motion of astrophysical sources on top of a complicated background.

E.O.O. is grateful for the support of grants from the Willner Family Leadership Institute, André De-loro Institute, Paul and Tina Gardner, The Norman E Alexander Family M Foundation ULTRASAT Data Center Fund, Israel Science Foundation, Israeli Ministry of Science, Minerva, BSF, BSF-transformative, NSF-BSF, Israel Council for Higher Education (VATAT), Sagol Weizmann-MIT, Yeda-Sela, and the Rosa and Emilio Segre Research Award. This research is supported by the Israeli Council for Higher Education (CHE) via the Weizmann Data Science Research Center, and by a research grant from the Estate of Harry Schutzman.

APPENDIX

SUFFICIENCY OF THE DIFFERENCE IMAGE STATISTIC \widehat{D}_T

Here we show that the difference image \widehat{D}_T defined in §2.4 is a *sufficient statistic* for determining the model parameters α_r , α_n , \vec{q} and \vec{p} . This is due to the fact that, given the model parameters, the PSF kernels P_r and P_n and the observational noise variances σ_r^2 and σ_n^2 (which we assume to be known), there is a one to one mapping between the difference image \widehat{D}_T (defined by Equation 24)

$$\widehat{D}_T \equiv \widehat{P}_r \widehat{N} - \widehat{P}_n \widehat{R} + \widehat{P}_n \widehat{P}_r (\alpha_r \widehat{\delta}_{\vec{q}} - \alpha_n \widehat{\delta}_{\vec{p}}), \quad (\text{A1})$$

and the *proper subtraction* image \widehat{D} defined by Equation (A21) of Zackay et al. (2016):

$$\widehat{D} \equiv \frac{\sqrt{\sigma_r^2 + \sigma_n^2} (\widehat{P}_r \widehat{N} - \widehat{P}_n \widehat{R})}{\sqrt{\sigma_n^2 |\widehat{P}_r|^2 + \sigma_r^2 |\widehat{P}_n|^2}}, \quad (\text{A2})$$

and therefore, $P(\widehat{D}_T | \alpha_r, \alpha_n, \vec{q}, \vec{p}) = P(\widehat{D} | \alpha_r, \alpha_n, \vec{q}, \vec{p})$. Moreover, Zackay et al. (2016) show that the proper subtraction image \widehat{D} is a sufficient statistic for determining the parameters of a family of generative processes which include the generative process of Equations 1 and 2. Hence, applying the result of Zackay et al. (2016) to our model parameters, we obtain

$$P(N, R | \alpha_r, \alpha_n, \vec{q}, \vec{p}) = P(\widehat{D} | \alpha_r, \alpha_n, \vec{q}, \vec{p}) h(R, N) \quad (\text{A3})$$

$$= P(\widehat{D}_T | \alpha_r, \alpha_n, \vec{q}, \vec{p}) h(R, N), \quad (\text{A4})$$

for some non-negative function h which does not depend on the model parameters. This, according to the Fisher-Neyman factorization theorem (Fisher 1922), characterizes \widehat{D}_T as a *sufficient statistic* with respect to the parameters α_r , α_n , \vec{q} , and \vec{p} . In practice, this means that

$$\log P(\widehat{D}_T | \alpha_r, \alpha_n, \vec{q}, \vec{p}) = \log P(N, R | \alpha_r, \alpha_n, \vec{q}, \vec{p}) + \text{const}, \quad (\text{A5})$$

where the additive constant does not depend on the model parameters.

REFERENCES

- Alard, C. and Lupton, R. H. (1998). A Method for Optimal Image Subtraction. *ApJ*, 503(1):325–331.
- Ben-Ami, S., Ofek, E. O., Polishook, D., Franckowiak, A., Hallakoun, N., Segre, E., Shvartzvald, Y., Strotjohann, N. L., Yaron, O., Aharonson, O., Arcavi, I., Berge, D., Fallah Ramazani, V., Gal-Yam, A., Garrappa, S., Hershko, O., Nir, G., Ohm, S., Rybicki, K., Segev, N., Shani, Y. M., Sofer-Rimalt, Y., and Weimann, S. (2023). The Large Array Survey Telescope – Science Goals. *arXiv e-prints*, page arXiv:2304.02719.
- Bramich, D. M. (2008). A new algorithm for difference image analysis. *MNRAS*, 386(1):L77–L81.
- Drake, A. J., Graham, M. J., Djorgovski, S. G., Catelan, M., Mahabal, A. A., Torrealba, G., García-Álvarez, D., Donalek, C., Prieto, J. L., Williams, R., Larson, S., Christen sen, E., Belokurov, V., Koposov, S. E., Beshore, E., Boattini, A., Gibbs, A., Hill, R., Kowalski, R., Johnson, J., and Shelly, F. (2014). The Catalina Surveys Periodic Variable Star Catalog. *ApJS*, 213(1):9.
- Fisher, R. A. (1922). On the Mathematical Foundations of Theoretical Statistics. *Philosophical Transactions of the Royal Society of London Series A*, 222:309–368.
- Foreman-Mackey, D., Hogg, D. W., Lang, D., and Goodman, J. (2013). emcee: The MCMC Hammer. *PASP*, 125(925):306.
- Ghez, A. M., Salim, S., Hornstein, S. D., Tanner, A., Lu, J. R., Morris, M., Becklin, E. E., and Duchêne, G. (2005). Stellar Orbits around the Galactic Center Black Hole. *ApJ*, 620(2):744–757.
- Gillessen, S., Eisenhauer, F., Trippe, S., Alexander, T., Genzel, R., Martins, F., and Ott, T. (2009). Monitoring Stellar Orbits Around the Massive Black Hole in the Galactic Center. *ApJ*, 692(2):1075–1109.
- Gould, A. (2000). Selection of Nearby Microlensing Candidates for Observation by the Space Interferometry Mission. *ApJ*, 532(2):936–942.
- Lindgren, L. (1980). Atmospheric limitations of narrow-field optical astrometry. *A&A*, 89(1-2):41–47.
- Liu, Y. (2015). Finding binary active galactic nuclei by the centroid shift in imaging surveys. *A&A*, 580:A133.
- Lu, J. R., Sinukoff, E., Ofek, E. O., Udalski, A., and Kozłowski, S. (2016). A Search For Stellar-mass Black Holes Via Astrometric Microlensing. *ApJ*, 830(1):41.
- Malkov, O. Y., Tamazian, V. S., Docobo, J. A., and Chulkov, D. A. (2012). Dynamical masses of a selected sample of orbital binaries. *A&A*, 546:A69.
- Neyman, J. and Pearson, E. S. (1933). On the Problem of the Most Efficient Tests of Statistical Hypotheses. *Philosophical Transactions of the Royal Society of London Series A*, 231:289–337.
- Ofek, E. O. (2014). MATLAB package for astronomy and astrophysics.
- Ofek, E. O. (2018). Toward the Measurement of the Mass of Isolated Neutron Stars: Prediction of Future Astrometric Microlensing Events by Pulsars. *ApJ*, 866(2):144.
- Ofek, E. O. (2019). A Code for Robust Astrometric Solution of Astronomical Images. *PASP*, 131(999):054504.
- Ofek, E. O., Ben-Ami, S., Polishook, D., Segre, E., Blumenzweig, A., Strotjohann, N. L., Yaron, O., Shani, Y. M., Nachshon, S., Shvartzvald, Y., Hershko, O., Engel, M., Segre, M., Segev, N., Zimmerman, E., Nir, G., Judkovsky, Y., Gal-Yam, A., Zackay, B., Waxman, E., Kushnir, D., Chen, P., Azaria, R., Manulis, I., Diner, O., Vandevanter, B., Franckowiak, A., Weimann, S., Borowska, J., Garrappa, S., Zenin, A., Fallah Ramazani, V., Konno, R., Küsters, D., Sadeh, I., Parsons, R. D., Berge, D., Kowalski, M., Ohm, S., Arcavi, I., and Bruch, R. (2023a). The Large Array Survey Telescope-System Overview and Performances. *PASP*, 135(1048):065001.
- Ofek, E. O., Shvartzvald, Y., Sharon, A., Tishler, C., Elhanati, D., Segev, N., Ben-Ami, S., Nir, G., Segre, E., Sofer-Rimalt, Y., Blumenzweig, A., Strotjohann, N. L., Polishook, D., Krassilchtchikov, A., Zenin, A., Fallah Ramazani, V., Weimann, S., Garrappa, S., Shanni, Y., Chen, P., and Zimmerman, E. (2023b). The Large Array Survey Telescope – Pipeline. I. Basic image reduction and visit coaddition. *arXiv e-prints*, page arXiv:2310.13063.

- Ofek, E. O. and Zackay, B. (2018). Optimal Matched Filter in the Low-number Count Poisson Noise Regime and Implications for X-Ray Source Detection. *AJ*, 155(4):169.
- Paczynski, B. (1998). Gravitational Microlensing with the Space Interferometry Mission. *ApJ*, 494(1):L23–L26.
- Phillips, A. C. and Davis, L. E. (1995). Registering, PSF-Matching and Intensity-Matching Images in IRAF. In Shaw, R. A., Payne, H. E., and Hayes, J. J. E., editors, *Astronomical Data Analysis Software and Systems IV*, volume 77 of *Astronomical Society of the Pacific Conference Series*, page 297.
- Sahu, K. C., Anderson, J., Casertano, S., Bond, H. E., Bergeron, P., Nelan, E. P., Pueyo, L., Brown, T. M., Bellini, A., Levay, Z. G., Sokol, J., aff1, Dominik, M., Calamida, A., Kains, N., and Livio, M. (2017). Relativistic deflection of background starlight measures the mass of a nearby white dwarf star. *Science*, 356(6342):1046–1050.
- Schechter, P. L., Mateo, M., and Saha, A. (1993). DoPHOT, A CCD Photometry Program: Description and Tests. *PASP*, 105:1342.
- Shao, M. and Colavita, M. M. (1992). Potential of long-baseline infrared interferometry for narrow-angle astrometry. *A&A*, 262(1):353–358.
- Shen, Y., Hwang, H.-C., Zakamska, N., and Liu, X. (2019). Varstrometry for Off-nucleus and Dual Sub-Kpc AGN (VODKA): How Well Centered Are Low-z AGN? *ApJ*, 885(1):L4.
- Soumagnac, M. T. and Ofek, E. O. (2018). catsHTM: A Tool for Fast Accessing and Cross-matching Large Astronomical Catalogs. *PASP*, 130(989):075002.
- Springer, O. M. and Ofek, E. O. (2021a). Measuring time delays: I. Using a flux time series that is a linear combination of time-shifted light curves. *arXiv e-prints*, page arXiv:2101.11017.
- Springer, O. M. and Ofek, E. O. (2021b). Measuring time delays: II. Using observations of the unresolved flux and astrometry. *arXiv e-prints*, page arXiv:2101.11024.
- Stetson, P. B. (1987). DAOPHOT: A Computer Program for Crowded-Field Stellar Photometry. *PASP*, 99:191.
- Zackay, B., Ofek, E. O., and Gal-Yam, A. (2016). Proper Image Subtraction—Optimal Transient Detection, Photometry, and Hypothesis Testing. *ApJ*, 830(1):27.